

The Discovery of an X-ray/UV Stellar Flare from the Late-K/Early-M dwarf LMC 335

B. T. H. Tsang¹

C. S. J. Pun¹

R. Di Stefano²

K. L. Li³

A. K. H. Kong^{1,3}

Received _____; accepted _____

¹Department of Physics, The University of Hong Kong, Pokfulam Road, Hong Kong

²Harvard-Smithsonian Center for Astrophysics, 60 Garden Street, Cambridge, MA 02138,
USA

³Institute of Astronomy and Department of Physics, National Tsing Hua University,
Hsinchu, Taiwan

ABSTRACT

We report the discovery of an X-ray/UV stellar flare from the source LMC 335, captured by *XMM-Newton* in the field of the Large Magellanic Cloud. The flare event was recorded continuously in X-ray for its first 10 hours from the precursor to the late decay phases. The observed fluxes increased by more than two orders of magnitude at its peak in X-ray and at least one in the UV as compared to quiescence. The peak 0.1–7.0 keV X-ray flux is derived from the two-temperature APEC model to be $\sim (8.4 \pm 0.6) \times 10^{-12} \text{ erg cm}^{-2} \text{ s}^{-1}$. Combining astrometric information from multiple X-ray observations in the quiescent and flare states, we identify the NIR counterpart of LMC 335 as the 2MASS source J05414534–6921512. The NIR color relations and spectroscopic parallax characterize the source as a Galactic K7–M4 dwarf at a foreground distance of (100 – 264) pc, implying a total energy output of the entire event of $\sim (0.4 - 2.9) \times 10^{35} \text{ erg}$. This report comprises detailed analyses of this late K / early M dwarf flare event that has the longest time coverage yet reported in the literature. The flare decay can be modeled with two exponential components with timescales of \sim 28 min and \sim 4 hours, with a single component decay firmly ruled out. The X-ray spectra during flare can be described by two components, a dominant high temperature component of \sim 40–60 MK and a low temperature component of \sim 10 MK, with a flare loop length of about 1.1–1.3 stellar radius.

Subject headings: Stars: activity – Stars: coronae – Stars: flare – Stars: individual LMC 335 – Stars: late-type – X-rays: stars

1. Introduction

Stellar flares from magnetically active stars provide useful tools to diagnose the physical processes governing the observed multi-wavelength characteristics, along with the physical and chemical evolutions of stellar coronae (Benz & Güdel 2010). Stars of spectral types F, G, K, and M are found to exhibit flare activities of various forms and scales. Dwarf flares have been extensively studied at wavelengths spanning from radio to X-ray, with UV and X-ray observations particularly effective for investigations of the cool dwarfs due to their characteristic ranges of coronal temperatures during flare (Osten et al. 2006; Berger et al. 2010). Many studies of flare stars have focused on the derivation of information about the magnetic activities associated with spatially unresolved flare events. The immense bursts of energy from stellar flares are believed to be generated from dynamo processes persistent in the stellar interiors and atmospheres. Hydrodynamic simulations (Reale et al. 1997; Favata et al. 2001; Allred et al. 2006) and the quasi-static radiative cooling models (van den Oord & Mewe 1989; Tsuboi et al. 2000) had been widely adopted to study the stellar magnetic activities based on their flare profiles.

Following the early detections of a small sample of flare candidates such as AT Mic and AD Leo (Kahn et al. 1979) with the HEAO-1 satellite, the *Einstein* and *EXOSAT* observatories extended the study to cover X-ray emission from stellar flares with better sensitivity and longer time coverage (Pallavicini et al. 1990). The observed energetic X-ray flares were divided into two subclasses based on the timescales of the flaring profiles: ‘impulsive’ flares with decay times of up to tens of minutes are believed to originate from relatively compact loops similar to those found on the sun; and ‘long-decay’ flares with typical hours-long decay time observed in solar two-ribbon flares (Priest & Forbes 2002). Pallavicini et al. (1990) observed 25 K5 to M7 stars within 25 pc with quiescent ($0.05\text{--}2\text{ keV}$) luminosities $\log L$ (erg s^{-1}) of ~ 27 – ~ 30 , and found X-ray flares with

energies from $\sim 3 \times 10^{30}$ to 1×10^{34} erg, and flare temperatures of $\sim 20\text{--}40$ MK. These values are comparable to those obtained from *Einstein* and these observations have extended the studies on stellar flares with improved sensitivity especially for their quiescent emissions.

In the extreme UV (EUV) wavelength, Mullan et al. (2006) conducted a survey on 44 type F to M stars in the Extreme UltraViolet Explorer (EUVE) database containing a total of 134 flares to explore the underlying dynamo mechanisms using physical parameters of the flare loops derived from a homogeneous set of flare lightcurves. The primary parameters investigated are the flare loop length and the magnetic fields during flares. It was suggested that the observed increase of maximum flare loop sizes from the warmer K2 to M0 sample to the cooler and later ones could be due to a transition from a core-convection dynamo to a turbulent dynamo.

After scattered *Einstein* and *EXOSAT* observations, the Röntgen Satellite (*ROSAT*) All-Sky Survey (RASS) provided a comprehensive coverage for the entire sky in soft X-ray. Tsikoudi et al. (2000) selected a sample of 14 active stars from K0 to M5.5 in the RASS database to search for concurrent energetic flares in both EUV and X-ray energies. Due to the observing strategy in the scanning mode, all the detected flares are of longer duration with event ages longer than an hour. High correlations of the X-ray (0.1–2.4 keV) and EUV (60–140 Å or 110–200 Å) luminosities could be deduced for all observed flares, with flare luminosities $\log L$ (erg s $^{-1}$) from 27.3 – 30.0 for X-ray, and 26.6 – 29.7 in EUV.

The better spatial and spectral resolution of the *XMM-Newton* and *Chandra* X-ray observatories vastly enhance the investigations of flare stars especially in the lower temperature end. Flare emissions from a number of dwarfs later than M8 were observed (Rutledge et al. 2000; Stelzer et al. 2006; Robrade & Schmitt 2009; Robrade et al. 2010; Gupta et al. 2011). These observations also enabled quiescent emission of late type stars to be detected and studied at much fainter limits, revealing the highly unstable nature during

quiescence, commonly referred to as quasi-quiescence states. Simultaneous monitoring in the X-ray and optical/UV wavelengths by *XMM-Newton* provide further constraints on the possible emission mechanisms associated with the magnetic activities. The availability of high-resolution X-ray spectroscopy supports the studies of coronal elemental abundances (Audard et al. 2003; Sanz-Forcada et al. 2004) as well as the construction of emission measure distribution during different stages of the flare evolution for detailed investigations of the temperature structure of the stellar coronae (Huenemoerder et al. 2001; Raassen et al. 2003).

The discovery of a previously unclassified flare object in the field of LMC by *XMM-Newton*, first detected in the quiescent state by the *ROSAT* High Resolution Imager (HRI) survey (Sasaki et al. 2000), is reported in this paper. The detected X-ray flare is found to be positioned at $\sim 2.5''$ from the catalogued position of source 335 (Sasaki et al. 2000), hereafter referred to as LMC 335. In addition to *ROSAT* and *XMM-Newton*, the source was also observed in X-ray quiescence with the *Chandra* and *Swift* satellites. In Section 2 the X-ray flare and quiescent observations of LMC 335, along with UV and optical images of the field, are described. Results of the findings are presented in Section 3: with Section 3.1 focusing on the source and counterpart identification, and Sections 3.2 and 3.3 on the timing and spectral analysis respectively. Discussions and conclusions are presented in Section 4.

2. Observations and data analysis

After the first detection by the *ROSAT HRI*, LMC 335 had been captured in X-ray with various instruments including *XMM-Newton*, *Chandra*, and *Swift*. Only one of

the *XMM-Newton* observations captured an X-ray/UV flare event, while all the other observations were made during quiescent states. Observational data in X-ray were obtained from the High Energy Astrophysics Science Archive Research Center (HEASARC) database. In this section we summarize the multiwavelength observations of LMC 335 and highlight those related to the flare event.

In Table 1 we list all the *XMM-Newton* European Photon Imaging Camera (EPIC) observations that included LMC 335. These observations were originally targeted at the pulsar PSR0540–69 and thus LMC 335 was at an off-axis angle of $\sim 9'$. The analysis was performed using the standard *XMM-Newton* Science Analysis System (SAS) version 11.0.0. With a majority of the quiescent state and flaring state X-ray photons contained in the lower energy bins, the energy band used for exposure map corrections and source detection was limited to 0.1 – 7.0 keV. At the position of LMC 335, source spectra were extracted with the SAS task *evselect* using a circular region of radius 10'', while the background was measured from a nearby source free circular region of radius 40'' on the same CCD. The same regions were adopted to generate lightcurves, with the task *epiclc* used to perform the background subtraction. All the spectra and response files were grouped with minimum counts of 20 and 10 for the flare duration and the quiescent phase respectively. The grouped spectra were then analyzed with XSPEC version 12.7.0.

The X-ray flare event from LMC 335 was recorded by the two *XMM-Newton* EPIC MOS cameras in medium optical filters on 2000 May 27 during a 40 ks observation (Obs.ID 0125120201 in Table 1). During the observation, while the central CCDs (CCD 1) of the two MOS cameras were operating in the Timing mode, the outer CCDs (CCD 2 – 7), where LMC 335 was captured, were in the Imaging mode. Unfortunately, the more sensitive EPIC PN camera was in the Small Window mode and did not include LMC 335 in its field of view. Therefore only data from two MOS cameras are available for the X-ray flare analysis.

In addition to the EPIC cameras, the Optical Monitor (OM) onboard *XMM-Newton* also recorded simultaneous UV broadband observations of LMC 335. Three of the ten *XMM-Newton* observations have OM imaging coverage, one of which was fortuitously taken during the flare. During the flaring observation, the OM took a series of UV images with filters UVW1 (245 – 320 nm), UVM2 (205 – 245 nm), and UVW2 (180 – 225 nm), with exposure time ranging from 1 ks to 4 ks. The exposures were all taken with the lateral Window 1 with 2×2 pixel binning. Details of the OM observations are summarized in Table 2. LMC 335 was not detected by the OM in the UV except for one UVW1 observation taken roughly 0.5 hours after the X-ray flux maximum. For the non-detections, the 3σ upper limits of count rates, magnitudes, and fluxes, were estimated with the average count rate computed from five source-free background regions near the source position. The detected magnitude was taken from the *omichain*-generated Observation Window (OSW) source lists. The magnitude to UV flux and upper limits conversion were done using the standard reference fluxes of Vega.

X-ray emission from the quiescent phase of LMC 335 was independently detected by the *Chandra* and *Swift* satellites in addition to *XMM-Newton*. In the case of *Chandra*, three HRC-I Non-grating observations of LMC 335 were taken in three separate pointings on 1999 August 31 (Obs.ID 132) and 2000 June 21 (Obs.IDs 1735 and 1736). The event lists were merged using the Chandra Interactive Analysis of Observations (CIAO) version 4.2 task *dmmerge* with an effective exposure time of \sim 48 ks. The observed quiescent count rate of $(3.4 \pm 0.5) \times 10^{-3} \text{ s}^{-1}$ was consistent with that measured by the *XMM-Newton*. On the other hand, the better angular resolution of the HRC data ($<0.5''$) provides more accurate position than the *XMM-Newton* MOS data ($2.0''$).

The field of LMC 335 had been imaged by *Swift* in a series of observations targeted also at PSR0540–69. A total of 22 sets of data were obtained spanning from 2005 April

to 2010 November with an integrated exposure time of \sim 170 ks. Similar to the *Chandra* observations, the data were taken when LMC 335 was in quiescent states and the X-ray emission was weak, with count rate of $(1.1 \pm 0.2) \times 10^{-3}$ counts $^{-1}$. The event lists were combined before lightcurves and spectra were extracted with the *Swift* tool *xrtgrblcspec*. A low signal-to-noise spectrum could be extracted from the combined event list, and was found to be consistent with (but of poorer quality than) the *XMM-Newton* data. The X-ray position and positional errors were computed using the task *xrtcentroid* for comparison with the other observations.

In addition to X-ray observations, archival optical/NIR data taken with European Southern Observatory Wide Field Imager (ESO-WFI) of LMC 335 are available through the observations of the association LH 104. The raw ESO-WFI images taken on 2004 November 21 were obtained from the ESO Archive¹ in four filters, *B* Bessel (ESO# 878), *Rc*/ 162 (ESO# 844), Z+60 (ESO# 846), and H_alpha 7 (ESO# 856), with cumulative exposure time of about 4, 2, 43, and 25 minutes respectively. With the reduced images, astrometry was done by registering five 2MASS and one Tycho bright stars near the field of LMC 335 with no known proper motions. The errors of the WCS mapping for all the ESO-WFI images are well below 0.1'' near the source LMC 335. Two catalogued sources, 2MASS J05414534–6921512 (Skrutskie et al. 2006) and DENIS J054145.2–692151 (DENIS Consortium 2005), are found to be closest to the position of LMC 335 and are considered to be the IR counterparts of the source. Since there is no systematic differences in *J* and *K_S* band measurements between 2MASS and DENIS (Cabrera-Lavers & Garzón 2003), the consistent *J* and *K_S* band magnitudes together with the slight positional offset of \sim 0.4'' of these two catalogued sources suggest that these counterparts are indeed the same physical object.

¹http://archive.eso.org/eso/eso_archive_main.html

3. Results

3.1. Source Position and Near-IR counterpart

Identification of counterparts of LMC 335 could reveal the nature of the X-ray flare event. Positions of the source computed from all the X-ray and IR data are listed with the $1-\sigma$ errors in Table 3. For the *Chandra* HRC data, the reported position for the source at quiescent state was obtained by the result obtained from image binning factors of 16. In the case of *XMM-Newton*, both the flare and quiescent state positions are reported. The two MOS flare detections were used to determine the flare state position while all other detections were used for quiescent state measurement. Before weight averaging the results from the individual detections, the $1-\sigma$ positional errors were obtained by combining in quadrature the statistical maximum likelihood (ML) fitting errors with the systematic error of the pointing of *XMM-Newton*, taken to be $2.0''$ (Guainazzi 2011) in this work. A similar approach of positional error calculation was adopted for the *XMM-Newton* Serendipitous source catalogue (Watson et al. 2009). With the best angular resolution, the *Chandra* HRC data provides the smallest uncertainty in the X-ray position of the source at its quiescent state, despite the low count rate recorded for the data. On the contrary, the low resolution of *Swift* and *ROSAT* data imply poor astrometry. The $1-\sigma$ uncertainty contours of the quiescent and flare states X-ray emission are overlaid on the ESO-WFI *Rc*-band image of the field in Figure 1, along with the catalogued positions of the two infrared counterparts 2MASS J05414534–6921512 and DENIS J054145.2–692151. The 2MASS position errors are too small to be presented as an error ellipse and its position is thus represented by a cross. It can be seen from Figure 1 that all X-ray detections are consistent in position with the uncatalogued ESO-WFI source that has IR counterparts from both the 2MASS and DENIS catalogues, with only slight deviation for the flare state detection position at $\sim 2''$ from the IR source positions. Offsets of similar extent were found with the other

X-ray bright source CAL 69 in the same *XMM-Newton* field, suggesting that the flare state position is compatible with the NIR counterparts identified.

In order to identify the nature of the source LMC 335, we studied the magnitudes and colors of the IR counterparts. The results are listed in Table 4. From its colors and magnitudes, it is possible to estimate the spectral type of LMC 335. Comparing our results with the 2MASS photometry of a filtered set of 461 K5 to M9.5 Galactic stars (Gelino et al. 2009), we found 90 K7 to M5.5 stars having 2MASS color indices lying within the error range reported in Table 4. The sources are mainly in the early M types, and has a median type of M2.5, with 95.6% (86/90) lying between K7 to M4. This is consistent with the Galactic K to M dwarfs identification we derived from the stellar population study along the direction to the LMC by Nikolaev & Weinberg (2000) using the 2MASS $J - K_S$ and K_S color-magnitude diagram. Using the spectroscopic parallax relation based on a sample of MLT dwarfs by Hawley et al. (2002), and assuming a spectral type of K7 to M4, the absolute M_J magnitude of the 2MASS counterpart is estimated to be 6.20–8.34, which transforms into a distance of 100–264 pc, with the median distance of 174 pc. Such estimation suggests the source is not in the LMC but is in the foreground. This distance range will be adopted as the distance to the object in the subsequent analyses of X-ray/UV emission.

3.2. Timing Analysis

The X-ray flare event of LMC 335 on 2000 May 27 was captured by the *XMM-Newton* MOS cameras in its entirety. The 0.1–7.0 keV background-subtracted X-ray lightcurve with 200 s binning is presented in the upper panel of Figure 2 (black: MOS1; red: MOS2). The time axis starts at 2000 May 27 UT 02:50 when the precursor phase (P) started, this will be referred to as the *flare start time* t_0 from hereafter. The quiescent state (Q) of the source

persisted during the first hour of observations with flux beneath our detection limit. Only a 3σ upper limit count rate of about $6 \times 10^{-3} \text{ s}^{-1}$ could be obtained. This is consistent with the expected average quiescent count rate computed from all other *XMM-Newton* MOS detections at $(4.0 \pm 0.7) \times 10^{-3} \text{ s}^{-1}$. The *Chandra* and *Swift* quiescent observations also produced consistent values, with PIMMS-converted (v4.4) *XMM-Newton* MOS count rates being $(5.7 \pm 0.9) \times 10^{-3}$ and $(3.9 \pm 0.6) \times 10^{-3}$ respectively, assuming a 1.1 keV (~ 12 MK) APEC plasma model (c.f. Table 5, Section 3.3). At ~ 1 hour after the start of the observation, the X-ray count rate suddenly rose to a precursor level (P) of $0.1 - 0.2 \text{ s}^{-1}$. At ~ 55 min after t_0 , the flare entered the rise (R) phase when the count rate rose sharply during ~ 800 s (~ 13 min) from the precursor level to over 1.1 s^{-1} at the flare peak. The flare flux then entered a decay phase starting 1.13 hours after t_0 and continuing until the end of the observation almost 10 hours later.

The OM provides simultaneous UV observations during the X-ray flare of LMC 335. Flux variation in the UV band during the flare is shown in Figure 2 (lower panel). Detailed detected count rate, magnitude, and flux, as well as the 3σ upper limits, are listed in Table 2. Only upper limits could be derived for the UVW1 observation taken during the quiescent phase of the flare, and the UVM2 data taken ~ 5 hours after t_0 . The only detection was the UVW1 image taken ~ 1.5 hours after t_0 during the Decay 1 (D1) phase, when a UV flux rose by at least one order of magnitude from the quiescent phase upper limit. Mitra-Kraev et al. (2005) studied the relation between X-ray and UV energy budget and found that the luminosity increases in X-ray and UV (measured in UVW1 band) during a stellar flare can be expressed as $\Delta L_X \propto \Delta L_{\text{UV}}^\alpha$, where $\alpha \sim 1.1 - 1.2$. While the time resolution of our UV data is not high enough for more detailed analysis, the observed flux increases in X-ray and UV are consistent with the power-law relation.

To facilitate a quantitative study of the behavior of the flare during the decay phase,

the lightcurve data points taken after $t_0 + 1.6$ hours were rebinned into intervals of 1000 s to give better statistics. The MOS1-MOS2 averaged count rates from the peak of emission 1.13 hours after t_0 are fitted with various exponential decay functions. We found that the data could be fit well with a two-component exponential decay function (reduced χ^2 , DOF = 1.01, 35) while the single-component model can be ruled out due to apparent deviation especially after the first hour of decay (reduced χ^2 , DOF = 17.07, 37). Initially the drop was rapid with an e-folding time (and $1-\sigma$ error) of $28.6^{+1.9}_{-1.3}$ min, the decay then slowed down to an e-folding time of $4.3^{+3.5}_{-0.6}$ hours. The X-ray lightcurve of the flare and the exponential fit are shown in Figure 3.

Based on the exponential fits to the X-ray lightcurve, we further divided the decay phase into the Decay 1 (D1) phase from the flare peak to include the first e-folding time of the fast decay component, followed by the Decay 2 (D2) phase until the end of the observations. The time boundaries of the Quiescence (Q), Precursor (P), Rise (R), Decay 1 (D1) and Decay (D2) phases are marked by black vertical dashed lines in Figure 3. To have a more detailed analysis of the conditions of the flare during its peak, an additional Flare (F) phase overlapping with R and D1, starting from 10.0 min before the peak to 23.4 min after flare peak, is defined as the interval during which the detected X-ray count rate is higher than half of the peak value (marked with dotted lines in Figure 3). The inset in Figure 3 shows a zoomed-in view of the lightcurve near the flare peak. At the beginning of phase D1, a slight excess in counts is observed at about 1.3 hours after t_0 , which could possibly come from another very brief rise phase after the main peak. Such multiple peak lightcurves had been detected in other stellar flares with comparable rise times (Pandey & Singh 2008; Welsh et al. 2007). On the other hand, this slight excess could certainly also have been resulted from the statistical fluctuations of the data.

This flare observation of LMC 335 was fortuitously captured near the beginning of a

long *XMM-Newton* exposure, thus allowing continuous observations of the first 10 hours of the flare event. From Figure 3, it is obvious that the X-ray emission still had not returned to the quiescent emission level by the end of the observation. The average MOS count rate for the last hour before the end of observations is $0.029 \pm 0.006 \text{ s}^{-1}$, which is a factor of 5 to 7 higher than the expected quiescent rate of 0.004 s^{-1} . This could originate from low-level flares persistent in the active regions after the main event.

3.3. X-ray Spectral Analysis

With the count rate at a low level for most of the duration of the flare, hardness ratios (HRs) were first computed to study the overall X-ray energy distribution of the event and to provide model-independent information for comparisons with other flares and other X-ray sources. The flare is soft, with X-ray photons in the energy range $0.1\text{--}2.0 \text{ keV}$ making up $\sim 80\%$ of all photons collected during the observation. The HR is defined as $\text{HR} = H/S$, where S and H are respectively the $0.1 - 2.0 \text{ keV}$ and $2.0 - 7.0 \text{ keV}$ count rates averaged from the MOS1 and MOS2 observations. Since LMC 335 was below the detection limit during the first hour of the flare *XMM-Newton* MOS observations, the HR for the quiescent phase is averaged from the non-flare PN *XMM-Newton* observations for proper comparison with the spectral fitting results. Figure 4 shows the time evolution of the HR of the flare during the five phases from pre-flare quiescence (Q) through the decay phases, with the flare phase (F) data point also shown for reference. We observed a sharp rise in HR from Q at 0.09 ± 0.05 to P phase of 0.45 ± 0.06 , reaching a maximum at phase R of 0.47 ± 0.05 . The value of HR then dropped through the F and the two decay phases, settling back near the quiescent level at 0.12 ± 0.01 for the D2 phase. The results imply that the flare in hard X-rays commenced simultaneously with the flare of the softer components, but decayed away much more quickly. This observed softening in X-ray after the R phase is common

among late-type stellar flares (Reale et al. 2004; Trenholme et al. 2004; Schmitt & Liefke 2002).

In addition to computing the hardness ratios, we have investigated the X-ray spectra of the flare in each phase. Identical procedures were followed for the generation of X-ray spectra in each phase except for the different numbers of minimum counts used to bin the spectra. The single-temperature (1T) and two-temperature (2T) thermal emission APEC models were used to analyze the spectra, except for the Q phase spectrum in which only the 1T model was carried out to derive a best-fit temperature of 1.22 keV (14.2 MK). The 2T model was found to provide better fits than the 1T model for all the other phases, with significant improvements for phase D1, D2, and F. As the fits were insensitive to the choice of metal abundance parameter, the Solar abundance was therefore used. The EM is derived from the normalization of the APEC model fitting in XSPEC and the assumed source distance range.

We observed that the high temperature components of ~ 5 keV emerged in the P and R phases, followed by a slight decline during the decay phases to ~ 3 keV while the low temperature components stayed at ~ 1 keV. The dominance of the hotter components is revealed from the consistently larger EM throughout the event as well as the biases in the fitted temperatures towards the hot range with the 1T model. Also, we observed an increase in EM for the cooler components above the quiescent value particularly in the R, D1, and F phases, which could be associated with the flare. Noticeable increases (by factors of $\sim 4 - 9$) in EM of the low temperature components from quiescence to flare peaks had been observed in other flares (Robrade et al. 2010; Gupta et al. 2011), but not as high as observed for this object (factor of ~ 23). Since the spectra from MOS1 and MOS2 are very similar, only the MOS1 spectra taken during each phase are shown in Figure 6. Data from the MOS1 and MOS2 were fitted together to provide better statistics and the quiescent

spectrum is obtained by previous non-flare PN observations. The best-fit parameters of the two models in different flare phases are summarized in Table 5 with all errors given in 90% confidence intervals as computed in XSPEC. The spectra had also been fitted by the equilibrium plasma model Mewe-Kaastra-Liedahl (MeKaL), resulting in similar best-fit parameters.

Due to the limited signals in the quiescent (Q) and the precursor (P) phases, the line-of-sight neutral hydrogen column density (n_{H}) could not be constrained by the fitting. Fixing n_{H} to values below 10^{21} cm^{-2} did not induce significant changes to the fitted plasma temperature, while the fits were poor (with reduced $\chi^2 \geq 3$) for n_{H} values above a few times of 10^{21} cm^{-2} . The n_{H} in quiescent and precursor states were thus fixed to be the average of the best-fits values from the two decay phases D1 and D2 at $0.67 \times 10^{20} \text{ cm}^{-2}$ for both the 1T and 2T models. The value from the rise phase (R) was not used for the estimation of n_{H} due to the unstable physical conditions during the period and the resulting bigger uncertainties of the fitted parameters. By using a fixed n_{H} in all phases, the other spectral parameters are similar to those obtained with floating n_{H} . The best-fit values of n_{H} from these spectra were about one order of magnitude lower than the weighted average values of hydrogen column density along that line-of-sight towards the LMC estimated from the Leiden/Argentine/Bonn (LAB) survey ($3.37 \times 10^{21} \text{ cm}^{-2}$) (Kalberla et al. 2005) and the Dickey & Lockman (DL) Galactic survey ($6.76 \times 10^{20} \text{ cm}^{-2}$) (Dickey & Lockman 1990). This provides additional supporting argument that the source is indeed located in the foreground instead of within the LMC.

The luminosity of LMC 335 at quiescent state $L_{\text{X,q}} = (0.2 - 1.7) \times 10^{29} \text{ erg s}^{-1}$ (0.1 – 7.0 keV) measured by *XMM-Newton* is comparable with the PIMMS implied value from the *ROSAT* HRI detected value of $2.4 \times 10^{29} \text{ erg s}^{-1}$ (0.1 – 2.4 keV) assuming the 1.1 keV APEC model as deduced for quiescence. *Chandra* and *Swift* observations also support

the relatively stable X-ray activity of the source in quiescence, with inferred luminosities of $1.8 \times 10^{29} \text{ erg s}^{-1}$ (0.08 – 10.0 keV) and $1.3 \times 10^{29} \text{ erg s}^{-1}$ (0.2 – 10.0 keV) respectively assuming the same spectral model.

Combining and averaging from the two MOS observations for the flare during the entire duration of observation, the flux of the source is $(8.8 \pm 0.4) \times 10^{-13} \text{ erg s}^{-1} \text{ cm}^{-2}$, implying a total emitted X-ray energy of $(0.4 - 2.9) \times 10^{35} \text{ erg}$ assuming a distance to the source of (100 – 264) pc and the total exposure time of 40 ks.

To characterize the X-ray activity, the $\log(L_X/L_{\text{bol}})$ ratios at different stages were computed and compared. To estimate the bolometric luminosities from the bolometric correction (BC) factor, the $\text{BC}_K-(J-K_S)$ relation derived from 51 M0–L7 stars with $0.75 \leq (J-K_S) \leq 1.60$ by Leggett et al. (2001) was used. To construct the BC relation, they computed the bolometric luminosities of the sample stars by integrating the observed IR spectra, with the short-wavelength ends linearly extrapolated to zero flux at zero wavelength and the long-wavelength ends approximated by the Rayleigh-Jeans tail. Using the IR colors of the 2MASS counterpart in Table 4, the BC_K was computed to be 2.63, and this transforms into an apparent bolometric magnitude of 15.10. Combining with the source distance of (100 – 264) pc, an absolute bolometric magnitude M_{bol} of (8.0 – 10.1) could be determined, implying the value of $\log(L_{\text{bol}}/L_{\odot})$ from –2.1 to –1.3. The range agrees closely with the estimates of –1.27 and –1.99 for M0/M1 and M3/M4 stars respectively in the *GALEX* M dwarfs UV flare survey (Welsh et al. 2007). The APEC model results were used for estimation of the total X-ray luminosity L_X to yield $\log(L_{X,q}/L_{\text{bol}}) = -3.1$ during quiescent state and $\log(L_{X,\text{flare}}/L_{\text{bol}}) = -0.4$ in the flare state, suggesting a significant rise in X-ray activity.

The evolution of the flare from quiescent to the decay phase is traced on the $\log T - \log \sqrt{EM}$ plane as shown in Figure 5. All the EM values were taken from the

dominant high-temperature components of the 2T spectral fits except for phase Q. Data points on Figure 5 are calculated based on the reference spectral type of M2.5 (174 pc), and the EM error bars includes only spectral fitting errors with XSPEC, while errors due to the uncertain source distance are not included. It is found that both the plasma temperature and EM increased significantly from Q to P phase. During the flare phases from P to D2, the temperature stayed roughly constant at $\sim (5 - 6) \times 10^7$ K while the EM fluctuated by about an order of magnitude around 10^{54} cm $^{-3}$. Similar evolution trends in both EM and temperature were also observed in the X-ray flare of the brown dwarf LP 412-31 (Stelzer et al. 2006) and the X-ray/optical flare of the late M dwarf Proxima Centauri (Reale et al. 2004). The relatively large errors of the spectral fitting prohibits more detailed studies of the evolution structure in the $\log T - \log \sqrt{EM}$ plane, but the general trend is clear. For source distances of 264 pc (K7) and 100 pc (M4), the relative positions between data points remains unchanged while the values on the EM axis offset by 0.18 and -0.24 respectively.

As the current signal-to-noise is not sufficient for detailed modeling, we studied the physical properties of the flare based on the Haisch's simplified approach (HSA) (Haisch 1983; Mullan et al. 2006). In this simplified parametrized scheme, the length of the flare loop can be estimated based only on the EM and the flare decay timescale τ_d . The loop lengths derived here represent the upper limits since multiple loops could be present while the numbers presented are for the single-loop scenario; together with the fact that the determined EM in the flare phase (F) should also include, albeit small, contributions from the precursor phase (P). In addition to the work by Mullan et al. (2006) with *EUVE*, Pandey & Singh (2012) adopted the HSA to study a number of X-ray flares from CVn-type binaries captured by *XMM-Newton*, while Schmitt et al. (1987) also tested the reliability of HSA with solar X-ray flares using EM values measured from *Einstein*. Using the D1 phase decay timescale derived from the MOS lightcurve and the sum of F phase EM , the

flare loop length during the F phase is estimated to be $(3.4 - 5.6) \times 10^{10}$ cm. Taking the stellar radii of M4 and K7 stars to be $0.4 R_{\odot}$ and $0.7 R_{\odot}$ (Lacy 1977; White et al. 1989; Ségransan et al. 2003), the size of the loop is estimated to be 1.1 – 1.3 times of the stellar radius. The range of the flare loop length in stellar radius is computed by the loop length and the stellar radius estimated for the associated spectral type. This is compatible with the picture that long-loop flares on main sequence stars occur mainly on M dwarfs as proposed by Mullan et al. (2006).

4. Discussion and Conclusions

In this paper we report the discovery and the multi-wavelength investigation of an X-ray/UV stellar flare from the K7 to M4 dwarf star LMC 335. The long, continuous X-ray observation of the source from the onset of the flare makes this event unique among those presented in the existing literature. While concurrent flare observations in X-ray and optical/UV bands had also been reported on later type M8 and M8.5 stars (Stelzer et al. 2006; Robrade et al. 2010), the current study is one of the best observed samples of late K and early M dwarfs with a full 11-hour X-ray coverage from quiescence to late decay phase together with a well observed precursor.

Quiescent emission from the source is found from multiple observations in X-ray, optical, and IR, with a counterpart identified in both the 2MASS and DENIS catalogues. The IR photometry and colors characterize the source as an K7 to M4 dwarf star, supporting the conclusion that the observed high energy flare originated from the stellar coronae. In quiescence, LMC 335 has an X-ray luminosity of $L_{X,q} \approx (0.2 - 1.7) \times 10^{29}$ erg s $^{-1}$ and a temperature of ~ 12 MK from the *XMM-Newton* data. The values are typical as for M dwarfs (Pallavicini et al. 1990; Schmitt et al. 1995; Schmitt & Liefke 2004), and are consistent with those deduced from both *Chandra* and *Swift* observations in quiescence.

The X-ray luminosity in quiescence and the bolometric luminosity of LMC 335 are found to be closely consistent with the K7 – M4 subsample studied by Pallavicini et al. (1990) and Tsikoudi et al. (2000). Moreover, the observed $\log(L_q/L_{\text{bol}})$ agree almost perfectly with the tight correlation of the two quantities deduced by Pallavicini et al. (1990) for late-K to M dwarfs, thus further confirming the K7–M4 classification of LMC 335. The distance of LMC 335 based on spectroscopic parallax and the n_{H} limit was estimated to be 100–264 pc. Consistent results obtained in the timing and spectral analysis with similar dwarf flares further strengthen the conclusion that LMC 335 is indeed in the foreground instead of residing in the LMC.

Clear precursor emission before the commencement of the main flare event was observed, with released X-ray energy of $\sim (0.5 - 3.2) \times 10^{34}$ erg, or about one-tenth of the total. Similar precursor phases have also been observed from the ultracool dwarf LP 412-31 (Stelzer et al. 2006) and from the Sun (Joshi et al. 2011), suggesting an intimate spatial relation between the pre-flare magnetically active regions and the main flare. The X-ray luminosity then sharply increased through the R phase to reach values of $(1.0 - 7.0) \times 10^{31}$ erg s $^{-1}$ and $(0.3 - 1.7) \times 10^{31}$ erg s $^{-1}$ in X-ray and UV, respectively. During the flare peak, the X-ray luminosity of LMC 335 was \sim 400 times higher than the quiescent value. The strongest increase recorded by Pallavicini et al. (1990) was only \sim 20, while more recently observed X-ray flares exhibited flux increases by factors ranging from few (Pandey & Singh 2008) to tens (Schmitt & Liefke 2002; Güdel et al. 2004; Stelzer et al. 2006; Wargelin et al. 2008; Robrade et al. 2010; Gupta et al. 2011), and up to hundreds (Favata et al. 2000; Fleming et al. 2000; Rutledge et al. 2000) to \sim 7000 (Osten et al. 2010). Furthermore, the quiescent luminosities of these sources ($10^{25} - 10^{28}$ erg s $^{-1}$) place LMC 335 at the energetic end of the X-ray flare samples. The loop length of LMC 335 is estimated from the HSA scheme to be comparable or bigger than the stellar radius, classifying our current flare under the ‘long loop’ category comparable to the \sim 1–3 times stellar radius

reported for less luminous flares (Schmitt & Liefke 2002; Mullan et al. 2006; Wargelin et al. 2008).

The long-time continuous X-ray coverage of the flare event allows for detailed lightcurve analysis. After the main flare peak, there could be a brief rise phase, arising possibly from the superposition of a less intense secondary flare on the main one. This could imply a more complicated spatial structure of the corona than the compact single-loop flaring scenario. More prominent multi-peak X-ray/UV flares had been observed for a number of G to K dwarfs (Pandey & Singh 2008) and M dwarfs (Welsh et al. 2007). For LMC 335, the drop in flux after the flare peak could be best characterized by a two-component exponential decay with e-folding timescales of \sim 28 min and \sim 4 hours, and the single-component decay model is ruled out. Similar two-stage flare decays were observed in some M dwarf X-ray flares including the M6 Proxima Centauri (Reale et al. 2004), M3.5 Ross 154 (Wargelin et al. 2008) and the M8 LP 412–31 (Stelzer et al. 2006). There are different interpretations of the change in decay timescale. Observations of large solar flares suggested that the slower decay may be resulted from the reconnected loops of the main flare which evolve differently (Aschwanden & Alexander 2001) or the overlapping with another ongoing flare event (Reale et al. 2004). On the other hand, there are flares in which single component decay models provide satisfactory fits. Their decay timescales range from \sim 0.1 ks to \gtrsim 10 ks. Finally, the observed count rate still exceeded the quiescent level by a factor of \sim 5 – 7 at the end of observation after nine hours of decay. Such late-time decay emission could be coming from continuous low level flare events occurring in the active regions left behind by the main flare.

The evolution of n_{H} at different phases cannot be constrained with the current dataset. Spectral fitting with two-temperature APEC model supports the parameterization of the flare spectra into a low-temperature component and a time-dependent high-temperature

flare component with similar spectral shapes and comparable parameters to other late M objects (Hambaryan et al. 2004; Stelzer et al. 2006; Robrade & Schmitt 2009; Robrade et al. 2010; Gupta et al. 2011). The cooler components (\sim 10 MK) are observed to have enhanced EM , along with the emergence of the hot components (\sim 60 MK) with EM of up to $(0.4 - 3.1) \times 10^{54} \text{ cm}^{-3}$ during flare peak. The total X-ray energy released is $\sim (0.4 - 2.9) \times 10^{35} \text{ erg}$. While only very few K7–M4 dwarf X-ray flares have been reported, the observed properties of LMC 335 place it at the energetic end of the limited sample.

The simultaneous UV observations show significant brightening in the UV band. Focusing primarily on the temporal coincidence between lightcurves in X-ray and UV, Mitra-Kraev et al. (2005) found an approximate time lag of \sim 10 minutes in X-ray. The low sampling rate of our UV data for LMC 335 could not confirm such possible lag. On the other hand, the lower limit of the X-ray to UV energy loss ratio derived for the quiescence phase and the ratio observed during the flare phase is consistent with the description of the quiescent state as the superposition of continuous low-energy small scale flares known as micro-flares (Parker 1988), or nano-flares depending on the timescales.

We would like to thank the anonymous referee for the helpful comments on the characterization of the spectral type of the source. B. T. H. Tsang acknowledges valuable discussions with Dr. Jifeng Liu and Dr. Frank Primini, and the support from HKU under the grant of Postgraduate Studentship. A. K. H. Kong gratefully acknowledges support from the National Science Council of the Republic of China (Taiwan) through grant NSC100-2628-M-007-002-MY3 and a Kenda Foundation Golden Jade Fellowship. This research has made use of data and software provided by the High Energy Astrophysics Science Archive Research Center (HEASARC), which is a service of the Astrophysics Science Division at NASA/GSFC and the High Energy Astrophysics Division of the Smithsonian Astrophysical Observatory. This research has also made use of the NASA/IPAC Infrared Science Archive, which is operated by the Jet Propulsion Laboratory, California Institute of Technology, under contract with the National Aeronautics and Space Administration. This was also supported by the use of observations made with the European Southern Observatory telescopes obtained from the ESO/ST-ECF Science Archive Facility. This investigation was supported by the RGC/GRF grant 704709 from the government of the Hong Kong SAR.

Table 1. X-ray detection of LMC 335 by the *XMM-Newton* EPIC

Obs.ID	Det-ExpID	Date (MM/DD/YYYY)	Start Time (UT HH:MM)	Exp. Time (ks)	Mode ^a	Opt. Fil.	Det. ML	Average Count Rate (s ⁻¹)
0113000401	M2S007	05/23/2001	07:33	47.8	PFW	Thick	24.4	0.0026
0117510201	PNS010 ^b	02/11/2000	09:05	10.8	PFW	Medium	55.2	0.0172
0117730501	M1S014	02/17/2000	13:29	10.2	PFW	Medium	20.8	0.0064
0117730501	M1S016	02/17/2000	17:20	14.2	PPW2	Medium	24.1	0.0051
0125120101	M1S008	05/26/2000	12:54	31.9	PFW	Medium	28.7	0.0034
0125120101	M2S010	05/26/2000	12:54	31.9	PFW	Medium	27.8	0.0035
0125120101	PNS006 ^b	05/26/2000	11:03	38.6	PFW	Medium	170.6	0.0159
0125120201	M1S007 ^c	05/27/2000	01:50	40.2	FastUC	Medium	6056.0	0.1218
0125120201	M2S009 ^c	05/27/2000	01:50	40.2	FastUC	Medium	6055.7	0.1193
0413180201	M2S002	10/02/2006	01:01	13.6	FastUC	Medium	9.0	0.0027
0413180301	M2S002	10/02/2006	18:36	16.2	FastUC	Medium	15.5	0.0033

^aScience mode of the central CCD. PFW: Prime Full Window; PPW2: Prime Partial W2 (small window); FastUC: Timing uncompressed. All detections here were made with imaging mode data.

^bXMM PN Observations capturing the quiescence, used for spectral analysis of quiescence (Q) phase (Table 5).

^cThe only XMM MOS Observations capturing the flare event, used for spectral analysis of the precursor (P), rise (R), decay 1 and 2 (D1-D2) and flare (F) phases (Table 5).

Table 2. UV detection of LMC 335 by the *XMM-Newton* Optical Monitor

OM Exp. ID	UV Filter	Start Time (UT HH:MM)	Exp. Time (s)	Count Rate (counts/s)	Magnitude	Flux (10 ⁻¹⁶ erg cm ⁻² s ⁻¹ Å ⁻¹)	Luminosity ^a (10 ³⁰ erg s ⁻¹)
0125120101 on 2000 May 26.							
440	UVW2	16:40	4000	≤ 0.07	≥ 17.7	≤ 4.2	≤ 2.3
0125120201 on 2000 May 27.							
432	UVW1	02:18	1000	≤ 0.38	≥ 18.3	≤ 1.8	≤ 1.4
436 [†]	UVW1	04:09	1000	3.81 ± 0.09	15.75 ± 0.03	(18.0 ± 0.5)	(2.5–17.4)
440	UVM2	07:39	2500	≤ 0.13	≥ 18.0	≤ 2.6	≤ 1.2
444	UVW2	13:14	4000	≤ 0.08	≥ 17.6	≤ 4.4	≤ 1.9
448	UVW2	18:44	2500	≤ 0.09	≥ 17.5	≤ 4.7	≤ 2.0
011300401 on 2001 May 23.							
401	UVM2	08:34	3500	≤ 0.12	≥ 18.1	≤ 2.6	≤ 1.5
404	UVM2	11:45	3500	≤ 0.11	≥ 18.2	≤ 2.3	≤ 1.4
405	UVW2	13:53	3500	≤ 0.08	≥ 17.6	≤ 4.6	≤ 2.5
408	UVW2	17:04	3500	≤ 0.07	≥ 17.7	≤ 4.2	≤ 2.3

Note. — 3- σ upper limits were computed for non-detections.

^aThe luminosity range is obtained by the assumed distance range of (100–264 pc), while the upper limits assumed the distance 264 pc

Table 3. Source positions of LMC 335 derived from X-ray and NIR instruments

Instrument	Detector	R.A. (J2000.0)	R.A. Error (arcsec)	Dec. (J2000.0)	Dec. Error (arcsec)
X-ray Positions					
<i>Chandra</i>	HRC-I	05 41 45.28	1.09	−69 21 51.5	1.0
<i>XMM-Newton</i> (Flare)	MOS	05 41 45.42	1.42	−69 21 49.4	1.4
<i>XMM-Newton</i> (Quiescent)	MOS + PN	05 41 45.29	0.86	−69 21 50.6	0.9
<i>Swift</i>	XRT-PC	05 41 45.35	3.60	−69 21 51.2	3.6
ROSAT	HRI	05 41 44.60	4.40	−69 21 51.1	4.4
NIR Positions					
2MASS		05 41 45.34	0.19	−69 21 51.22	0.1
DENIS		05 41 45.27	≤ 1	−69 21 51.10	≤ 1

Note. — NIR counterparts are 2MASS J05414534−6921512 and DENIS J054145.2−692151.

Table 4. NIR magnitudes and colors of the 2MASS and DENIS counterparts

2MASS Counterpart	<i>J</i>	<i>H</i>	<i>K_S</i>
	<i>J</i> − <i>H</i>	<i>H</i> − <i>K_S</i>	<i>J</i> − <i>K_S</i>
2MASS J05414534−6921512	13.31 ± 0.04	12.68 ± 0.05	12.47 ± 0.04
	0.63 ± 0.06	0.21 ± 0.06	0.84 ± 0.06
DENIS Counterpart	<i>I</i>	<i>J</i>	<i>K_S</i>
	<i>I</i> − <i>J</i>	<i>J</i> − <i>K_S</i>	<i>I</i> − <i>K_S</i>
DENIS J054145.2−692151 (a)	14.38 ± 0.03	13.19 ± 0.08	12.41 ± 0.14
	1.20 ± 0.09	0.78 ± 0.16	1.98 ± 0.14
DENIS J054145.2−692151 (b)	14.34 ± 0.03	13.20 ± 0.07	12.16 ± 0.11
	1.14 ± 0.08	1.04 ± 0.13	2.18 ± 0.11

Table 5. Spectral Fitting Results of LMC 335’s flare with the *XMM-Newton* detections

Stage	Duration $t_0 +$ (Hours)	n_H (10^{20} cm^{-1})	kT (keV)	χ^2_ν (D.O.F.)	EM^c (10^{52} cm^{-3})	Flux ^d ($10^{-13} \text{ erg cm}^{-2} \text{ s}^{-1}$)	Luminosity ^{c,d} ($10^{29} \text{ erg s}^{-1}$)
1T APEC Model Results							
Q ^a	0.67 ^b	1.22 ^{+0.11} -0.23	1.36 (22)	(0.1 – 0.7)	(0.21 ± 0.03)	(0.2 – 1.7)
P	0.00 – 0.90	0.67 ^b	4.33 ^{+2.27} -1.13	1.61 (10)	(6.7 – 46.5)	(11.2 ± 1.8)	(13.3 – 92.9)
R	0.90 – 1.13	2.09 ^{+2.13} -1.45	4.88 ^{+1.88} -1.14	0.99 (17)	(47.4 – 330)	(82.0 ± 9.8)	(97.7 – 681)
D1	1.13 – 1.59	0.71 ^{+0.79} -0.60	3.95 ^{+0.62} -0.55	1.44 (37)	(42.4 – 295)	(70.0 ± 5.5)	(83.4 – 581)
D2	1.59 – 10.10	0.57 ^{+0.50} -0.40	3.29 ^{+0.30} -0.27	1.94 (60)	(4.1 – 28.8)	(6.6 ± 0.4)	(7.8 – 54.6)
F	0.96 – 1.52	1.23 ^{+0.75} -0.60	4.29 ^{+0.71} -0.48	1.19 (49)	(49.5 – 345)	(83.4 ± 5.6)	(99.4 – 693)
2T APEC Model Results							
P	0.00 – 0.90	0.67 ^b	0.28 ^{+1.20} -0.28	1.45 (8)	(0.4 – 2.8)	(11.7 ± 2.1)	(14.0 – 97.4)
			5.21 ^{+2.47} -1.82		(6.1 – 42.6)		
R	0.90 – 1.13	1.91 ^{+1.92} -1.35	1.01 ^{+3.32} -0.69	0.98 (15)	(1.5 – 10.2)	(83.2 ± 10.1)	(99.5 – 693)
			5.83 ^{+2.31} -1.25		(44.2 – 308)		
D1	1.13 – 1.59	0.67 ^{+0.88} -0.63	0.95 ^{+0.13} -0.17	0.93 (35)	(2.6 – 18.2)	(70.8 ± 5.8)	(84.7 – 591)
			4.66 ^{+1.39} -0.80		(36.9 – 257)		
D2	1.59 – 10.10	0.67 ^{+0.57} -0.45	0.76 ^{+0.10} -0.16	1.09 (58)	(0.3 – 1.8)	(6.7 ± 0.40)	(8.0 – 55.6)
			3.61 ^{+0.49} -0.36		(3.6 – 25.1)		
F	0.96 – 1.52	1.14 ^{+0.80} -0.63	1.06 ^{+0.28} -0.22	0.99 (47)	(2.3 – 16.1)	(84.2 ± 5.9)	(101 – 702)
			5.07 ^{+1.61} -0.86		(44.8 – 312)		

Note. — The error ranges of all parameters give the 90% confidence intervals.

^aThe spectral properties are derived from previous non-flare PN observations, as listed in Table 1.

^bThe value was fixed to the average of the Decay stages’ in the 2T model.

^cParameter are shown in ranges correponding to source distance of 100–264 pc.

^dX-ray fluxes and luminosities are for the 0.1 – 7.0 keV band.

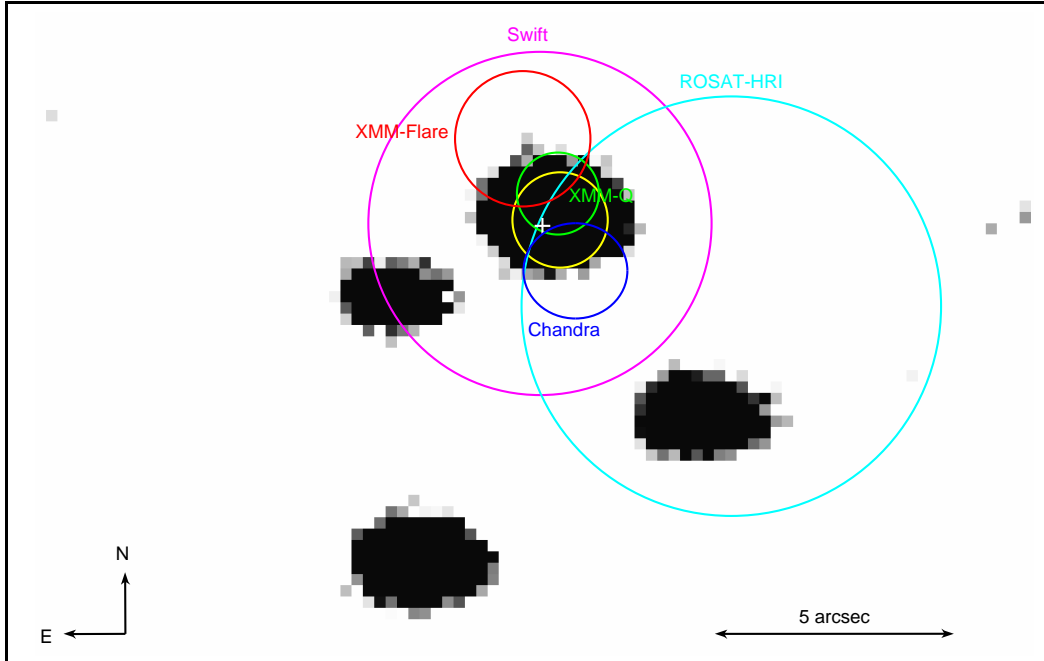


Fig. 1.— ESO WFI R_c band image of the LMC 335 field shown with NIR and X-ray source positions and $1-\sigma$ error circles. White cross: 2MASS J05414534–6921512 counterpart, yellow circle: DENIS J054145.2–692151 counterpart, red circle: weighted average position from *XMM-Newton* flare observations, green circle: weighted average position from the *XMM-Newton* quiescent observations, blue circle: *Chandra* HRC position, cyan circle: *ROSAT* HRI position, magenta circle: *Swift* XRT positon.

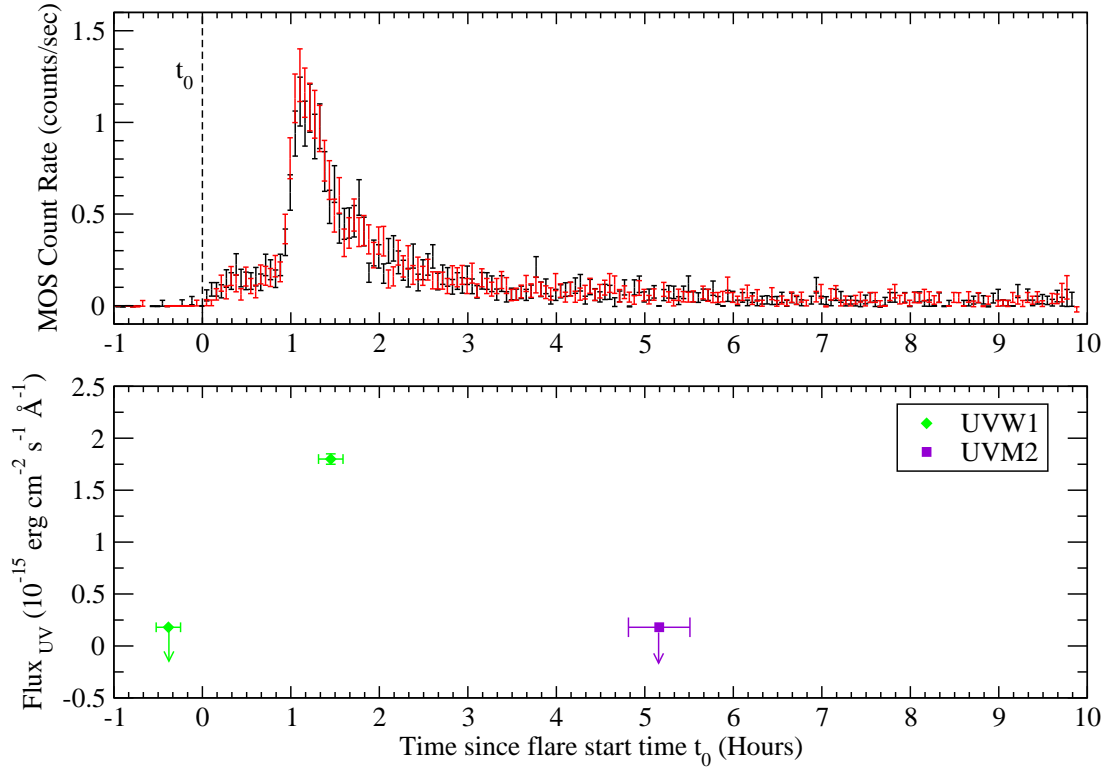


Fig. 2.— *Upper panel:* *XMM-Newton* EPIC MOS background subtracted lightcurves (black: MOS1, red: MOS2) of LMC 335 in 0.1–7.0 keV band throughout the flare event. Time $t = 0$ corresponds to 2000 May 27 UT 02:50, the flare start time denoted by t_0 . Time bins used are 200 s. *Lower panel:* The *XMM-Newton* OM-derived UV fluxes/upper limits in the corresponding filters during the X-ray observations.

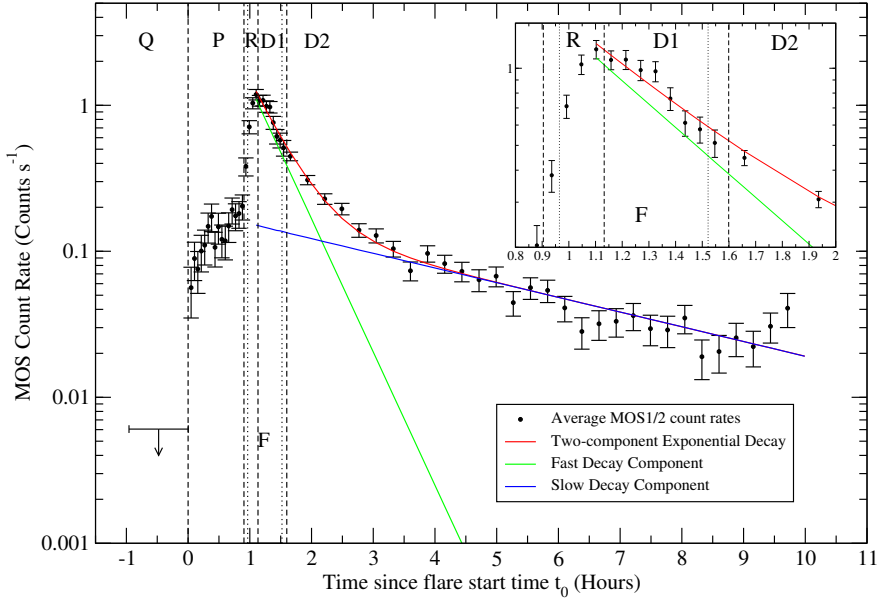


Fig. 3.— MOS1 and MOS2 averaged lightcurve of LMC 335 is replotted in logarithmic scale overlaid with the exponential fits. Time $t = 0$ refers to 2000 May 27 UT 02:50, the flare start time t_0 as denoted in Figure 2. The observation is partitioned into five phases: quiescence (Q), precursor (P), rise (R), decay 1 and 2 (D1–D2) marked by black dashed lines. The additional flare (F) phase bounded by dotted lines is added to study the properties of LMC 335 during the peak state. The time bins for D2 have been widened from 200 s to 1000 s for better statistics and visualization. Detailed evaluation of the lightcurve near the flare peak is shown in the inset figure.

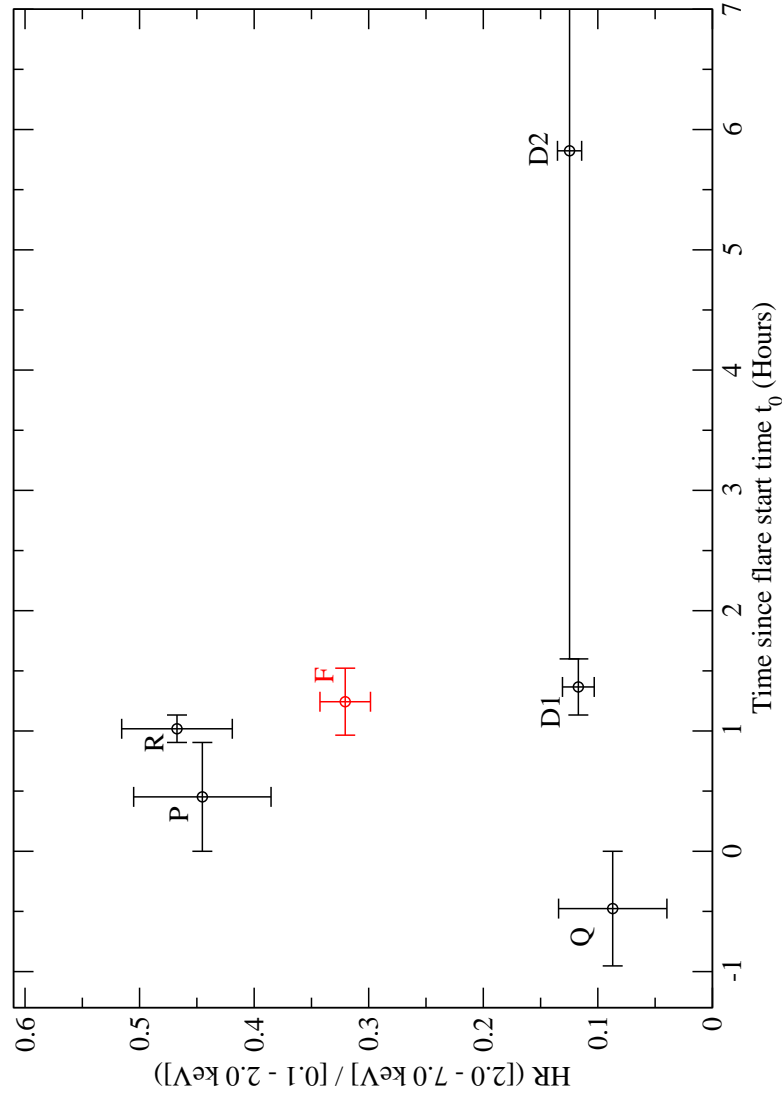


Fig. 4.— Evolution of X-ray Hardness Ratio (HR) during the six representative phases from quiescence (Q) to decay 2 (D2). The averaged HR from the non-flare PN *XMM-Newton* observations is used to represent phase Q.

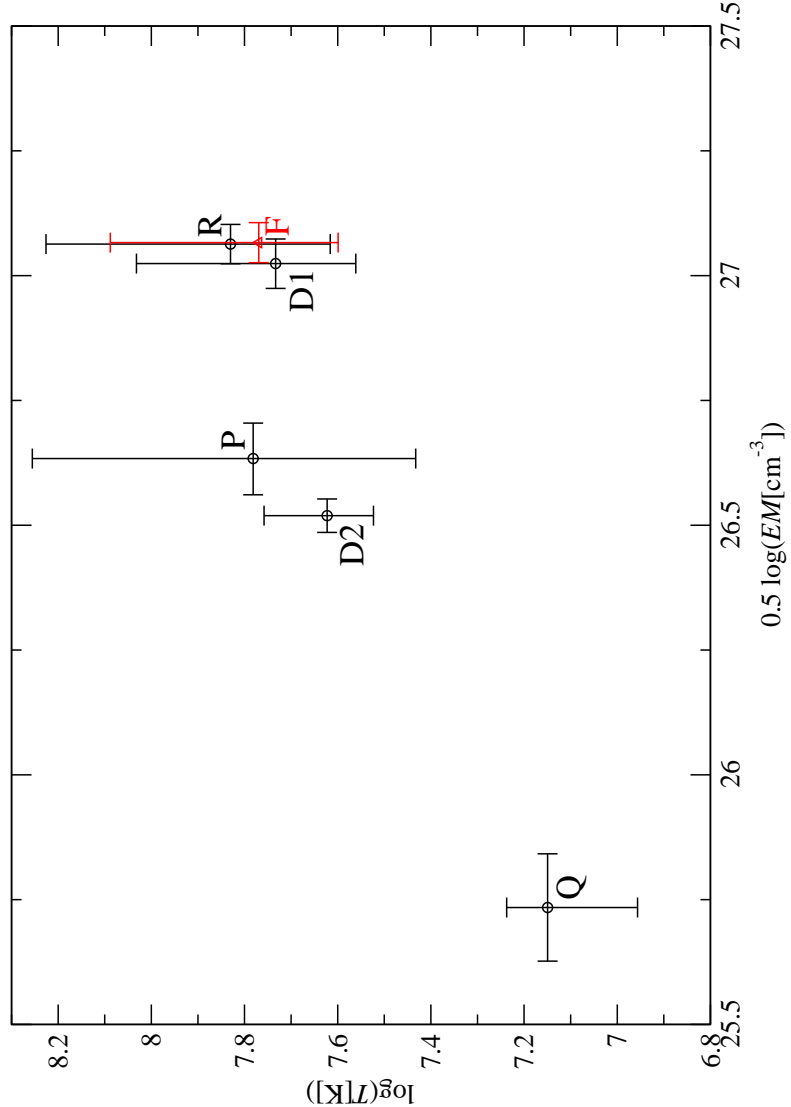


Fig. 5.— Time evolution of temperature and the Emission Measure (EM) during the six representative phases from quiescence (Q) to decay 2 (D2) as derived for a reference spectral type of M2.5 (174 pc). The data point for quiescent phase is derived from the 1T APEC model; parameters for all other phases are obtained from the high-temperature components of the 2T APEC fits. The error bars for the EM values include only the uncertainties in XSPEC normalization, the uncertainty in source distance is not included. For spectral types of K7 (264 pc) and M4 (100 pc), the values on the EM axis offset by 0.18 and -0.24 respectively with the relative positions of data points unchanged.

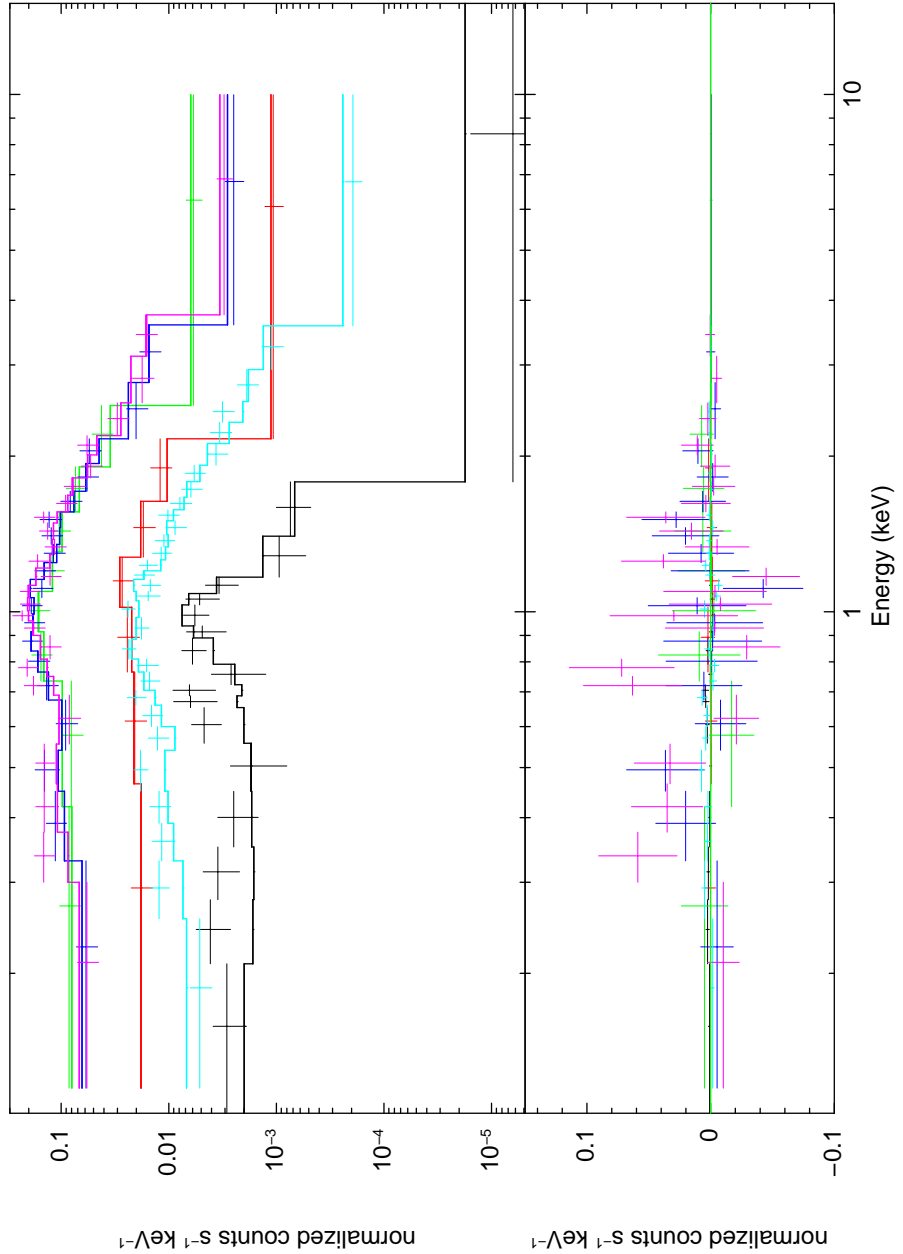


Fig. 6.— *XMM-Newton* MOS1 background subtracted spectra with best fit 1T APEC model for quiescence (black); and 2T APEC model for precursor (red), rise (green), decay 1 (blue), decay 2 (cyan), and flare (magenta) phases.

REFERENCES

- Allred, J. C., Hawley, S. L., Abbott, W. P., & Carlsson, M. 2006, ApJ, 644, 484
- Aschwanden, M. J., & Alexander, D. 2001, Sol. Phys., 204, 91
- Audard, M., Güdel, M., Sres, A., Raassen, A. J. J., & Mewe, R. 2003, A&A, 398, 1137
- Benz, A. O., & Güdel, M. 2010, ARA&A, 48, 241
- Berger, E., et al. 2010, ApJ, 709, 332
- Cabrera-Lavers, A., & Garzón, F. 2003, A&A, 403, 383
- DENIS Consortium. 2005, VizieR Online Data Catalog, 2263, 0
- Dickey, J. M., & Lockman, F. J. 1990, ARA&A, 28, 215
- Favata, F., Micela, G., & Reale, F. 2001, A&A, 375, 485
- Favata, F., Reale, F., Micela, G., Sciortino, S., Maggio, A., & Matsumoto, H. 2000, A&A, 353, 987
- Fleming, T. A., Giampapa, M. S., & Schmitt, J. H. M. M. 2000, ApJ, 533, 372
- Gelino, C. R., Kirkpatrick, J. D., & Burgasser, A. J. 2009, in American Institute of Physics Conference Series, Vol. 1094, American Institute of Physics Conference Series, ed. E. Stempels, 924–927
- Guainazzi, M. 2011, XMM-Newton Calibration Technical Note, Tech. Rep. XMM-SOC-CAL-TN-0018, ESA-ESAC, Villafranca del Castillo, Spain
- Güdel, M., Audard, M., Reale, F., Skinner, S. L., & Linsky, J. L. 2004, A&A, 416, 713
- Gupta, A., Galeazzi, M., & Williams, B. 2011, ApJ, 731, 63

- Haisch, B. M. 1983, in IAU Colloq. 71, Activity in Red Dwarf Stars, ed. Byrne, P. B., Rodono, M., 255
- Hambaryan, V., Staude, A., Schwope, A. D., Scholz, R.-D., Kimeswenger, S., & Neuhäuser, R. 2004, A&A, 415, 265
- Hawley, S. L., et al. 2002, AJ, 123, 3409
- Huenemoerder, D. P., Canizares, C. R., & Schulz, N. S. 2001, ApJ, 559, 1135
- Joshi, B., Veronig, A. M., Lee, J., Bong, S.-C., Tiwari, S. K., & Cho, K.-S. 2011, ApJ, 743, 195
- Kahn, S. M., Mason, K. O., Bowyer, C. S., Linsky, J. L., Haisch, B. M., White, N. E., & Pravdo, S. H. 1979, ApJ, 234, 107
- Kalberla, P. M. W., Burton, W. B., Hartmann, D., Arnal, E. M., Bajaja, E., Morras, R., & Pöppel, W. G. L. 2005, A&A, 440, 775
- Lacy, C. H. 1977, ApJS, 34, 479
- Leggett, S. K., Allard, F., Geballe, T. R., Hauschildt, P. H., & Schweitzer, A. 2001, ApJ, 548, 908
- Mitra-Kraev, U., et al. 2005, A&A, 431, 679
- Mullan, D. J., Mathioudakis, M., Bloomfield, D. S., & Christian, D. J. 2006, ApJS, 164, 173
- Nikolaev, S., & Weinberg, M. D. 2000, ApJ, 542, 804
- Osten, R. A., Hawley, S. L., Allred, J., Johns-Krull, C. M., Brown, A., & Harper, G. M. 2006, ApJ, 647, 1349
- Osten, R. A., et al. 2010, ApJ, 721, 785

- Pallavicini, R., Tagliaferri, G., & Stella, L. 1990, A&A, 228, 403
- Pandey, J. C., & Singh, K. P. 2008, MNRAS, 387, 1627
- . 2012, MNRAS, 419, 1219
- Parker, E. N. 1988, ApJ, 330, 474
- Priest, E. R., & Forbes, T. G. 2002, A&A Rev., 10, 313
- Raassen, A. J. J., Mewe, R., Audard, M., & Güdel, M. 2003, A&A, 411, 509
- Reale, F., Betta, R., Peres, G., Serio, S., & McTiernan, J. 1997, A&A, 325, 782
- Reale, F., Güdel, M., Peres, G., & Audard, M. 2004, A&A, 416, 733
- Robrade, J., Poppenhaeger, K., & Schmitt, J. H. M. M. 2010, A&A, 513, A12
- Robrade, J., & Schmitt, J. H. M. M. 2009, A&A, 496, 229
- Rutledge, R. E., Basri, G., Martín, E. L., & Bildsten, L. 2000, ApJ, 538, L141
- Sanz-Forcada, J., Favata, F., & Micela, G. 2004, A&A, 416, 281
- Sasaki, M., Haberl, F., & Pietsch, W. 2000, A&AS, 143, 391
- Schmitt, J. H. M. M., Fink, H., & Harnden, Jr., F. R. 1987, ApJ, 322, 1023
- Schmitt, J. H. M. M., Fleming, T. A., & Giampapa, M. S. 1995, ApJ, 450, 392
- Schmitt, J. H. M. M., & Liefke, C. 2002, A&A, 382, L9
- . 2004, A&A, 417, 651
- Ségransan, D., Kervella, P., Forveille, T., & Queloz, D. 2003, A&A, 397, L5
- Skrutskie, M. F., et al. 2006, AJ, 131, 1163

- Stelzer, B., Schmitt, J. H. M. M., Micela, G., & Liefke, C. 2006, A&A, 460, L35
- Trenholme, D., Ramsay, G., & Foley, C. 2004, MNRAS, 355, 1125
- Tsikoudi, V., Kellett, B. J., & Schmitt, J. H. M. M. 2000, MNRAS, 319, 1136
- Tsuboi, Y., Imanishi, K., Koyama, K., Grossi, N., & Montmerle, T. 2000, ApJ, 532, 1089
- van den Oord, G. H. J., & Mewe, R. 1989, A&A, 213, 245
- Wargelin, B. J., Kashyap, V. L., Drake, J. J., García-Alvarez, D., & Ratzlaff, P. W. 2008, ApJ, 676, 610
- Watson, M. G., et al. 2009, A&A, 493, 339
- Welsh, B. Y., et al. 2007, ApJS, 173, 673
- White, S. M., Jackson, P. D., & Kundu, M. R. 1989, ApJS, 71, 895